Structural and magnetic properties of $NiFe_2O_4$/NiFe bi-magnet and NiFe nano-alloy synthesized from thermal reduction of $NiFe_2O_4$

Itegbeyogene P Ezekiel [1], **Thomas Moyo and Hafiz M I Abdallah**
School of Chemistry and Physics, University of KwaZulu-Natal, P/Bag X5400, Durban 4000, South Africa

E-mail: itegbeyogene@gmail.com

Abstract. $NiFe_2O_4$/NiFe nanocomposites, NiFe nano-alloy were synthesized by reduction of $NiFe_2O_4$ nano-ferrite with activated charcoal under Ar gas atmosphere at 900 °C for 3 hours. The $NiFe_2O_4$ was synthesized by a glycol-thermal. Partial and complete reduction yielded $NiFe_2O_4$/NiFe and NiFe, respectively. NiFe was formed at an optimum amount of activated charcoal of n_c = 5. Phase identification, morphology and magnetic properties were performed by X-ray diffraction (XRD), high-resolution scanning electron microscope, ^{57}Fe Mössbauer spectroscope and mini cryogenic-free system. $NiFe_2O_4$ has an average crystallite size of 10 nm, an XRD density of 5.3 g/cm^3 and an average lattice parameter of a = 8.362 ± 0.007 Å. NiFe exhibited the martensite bcc (α-Fe) and austenite fcc (γ-Fe) phases in coexistence with average a of 2.867±0.001 Å and 3.580±0.001 Å, respectively. Fitted Mössbauer analysis for n_c = 5 and 6 show high hyperfine magnetic fields associated with the bcc phase while the lower field component is associated with the fcc phase of NiFe. The saturation magnetization increased significantly from 57 emu/g to 141 emu/g at room temperature. The saturation magnetization is enhanced at low temperatures with a maximum of 161 emu/g at ≥ 30 K. The coercivity showed no significant increase at low temperatures.

1. Introduction

Research efforts for scalable and efficient synthesis method of nano-materials have increased in recent times. This has happened mainly because of targeted properties of these materials for specific applications in areas such as catalysis, ferrofluids, drug delivery, microwave devices, laser cavity, gas-sensor, magnetic recording and dimension stabilizers [1, 2]. Nano-ferrites and their nanocomposites are promising and attractive materials for most of these applications. Nickel nano-ferrite ($NiFe_2O_4$) is a typical example of such material. $NiFe_2O_4$ is a soft magnetic material [3] with Ni having much lower anisotropy effect compared to cobalt Co. $NiFe_2O_4$ has an inverse spinel structure where the Ni^{2+} ions are located in octahedral sites and the Fe^{3+} ions located both in octahedral (B) and tetrahedral (A) sites [4]. The location of the divalent cations has a relationship with the magnetic properties. The nanocomposite of $NiFe_2O_4$/NiFe is expected to exhibit an enhanced magnetization due to the synergetic saturation magnetization arising from the ferrite and alloy phases. The alloy phase within an appropriate composition shows some interesting anomalous thermal and magnetic properties [5] for

[1] To whom any correspondence should be addressed.

suitable applications. The improvement of these soft magnetic materials to maintain high saturation, permeability, resistivity and relative stability in air is paramount. Hu *et al* [6] reported the synthesis and characterization of $NiFe_2O_4$/NiFe nanocomposites synthesized by colloidal chemical method combined with hydrogen (H_2) reduction with a relatively low magnetization. In our research, we report the synthesis of our parent sample to be $NiFe_2O_4$ nano-ferrite, NiFe as the nano-alloy and $NiFe_2O_4$/NiFe bi-magnetic nanocomposites. The as-prepared sample was synthesized by a glycol-thermal method and reduced with activated charcoal. The use of activated charcoal is cheap and safer compared to the use of H_2. The nanocomposite synthesis of $NiFe_2O_4$/NiFe by reduction using activated charcoal on $NiFe_2O_4$ nano-ferrite has not been reported. A strong interest in investigating the improved magnetic and structural properties arising from these synthesis methods informed this research. These properties were investigated using X-ray powder diffraction, high-resolution scanning electron microscope, ^{57}Fe Mössbauer spectroscope and a mini cryogenic-free system.

2. Experimental details

$NiFe_2O_4$ was synthesized by the glycol-thermal method [7]. $NiFe_2O_4$ was reduced with specific amounts of carbon n_c = 1, 2, 4, 5, 6, 8 and 10 to produce $NiFe_2O_4$/NiFe and /NiFe based on this equation; $NiFe_2O_4 + n_cC \rightarrow NiFe + n_cCo_2$, for 0.5g fixed mass of NiFe2O4. The reductions were performed at 900 °C for 3 hours in argon atmosphere. XRD, high resolution scanning electron microscope (HRSEM), ^{57}Fe Mössbauer spectroscope and a mini cryogen free system was used to characterize the samples.

3. Results and discussion

The X-ray diffraction (XRD) patterns for $NiFe_2O_4$ nano-ferrite, $NiFe_2O_4$/NiFe nanocomposites and NiFe nano-alloy formed with various amounts of activated charcoal (n_c) are shown in Figure 1. The pure nano-ferrite at n_c = 0 conforms to the cubic spinel structure of bulk $NiFe_2O_4$ (JCPDS Card No. 10-0325) [1]. All the peaks are indexed with respect to Miller indices (111), (220), (311), (400), (422), (511) and (440) without evidence of any impurity peaks. The crystallite size (G) was calculated using the Scherrer's formula with the full-width at half-maximum (w_{hkl}) of the line broadening diffraction peak derived from the most prominent (311) peak of the $NiFe_2O_4$. The shape factor K is equal to 1, λ is the wavelength of a CoKα source monochromatic X-ray beam and θ is the Bragg's angle. The X-ray density of the ferrite calculated using; $\rho_{XRD} = 8M/N_A a^3$ where M is the molecular weight, N_A is the Avogadro's number and a is the lattice parameter [7]. The crystallite size and the X-ray density of $NiFe_2O_4$ was estimated to be G = 10.48±0.08 nm and 5.3±0.1 g/cm^3 respectively. The value of the lattice parameter of this compound was calculated from the (311) peak to be a = 8.362±0.007 Å using $a = \lambda/2\sin\theta\sqrt{(h^2 + k^2 + l^2)}$ where h, k, and l are the Miller indices. This is close to a reported value of 8.339 Å [1]. The XRD diffraction results show that partial reduction occurs for n_c = 1 to 4 for activated charcoal to yield $NiFe_2O_4$/NiFe nanocomposites. The small unidentified peak close to the (311) peak when n_c = 1 is attributed to a possible transient impure phase which eventually disappears for n_c > 4. Complete reduction of the ferrite phase to NiFe nano-alloy to form fcc and bcc phases [8] occurs for at least n_c > 4. The presence of FeO for n_c = 1 to 4 is attributed to the possibility of still unreacted iron ions in the sample crystallite interior with the activated charcoal atoms reacting most effectively with surface nano-ferrites. In all reduced samples, NiFe nano-alloy phase shows the coexistence of the austenite γ-Fe fcc (Ni-rich) indexed to the (111) peak and the martensite α-Fe bcc (Fe-rich) lattice structures indexed to the (110) peak [9]. The fcc and bcc crystallite sizes G were calculated from the (111) and (110) peaks, respectively. The abrupt growth in the crystallite size at n_c = 2 could be influenced by the most prominent presence of FeO phase at n_c = 2. The (200) peak has a lattice parameter associated with the fcc lattice structure with a value of a = 3.585 Å. The values of the lattice parameter suggest the nano-alloy composition to be Fe-Ni at 42 % Ni [10] because around this composition the lattice parameter expands from 3.572 Å to 3.588 Å at room temperature. The (111) γ-Fe peak has the most predominant crystalline phase with no obvious change in peak growth compared to the bcc α-Fe phase. Figure 2 shows that crystallite size of the bcc phase is smaller with a continuous

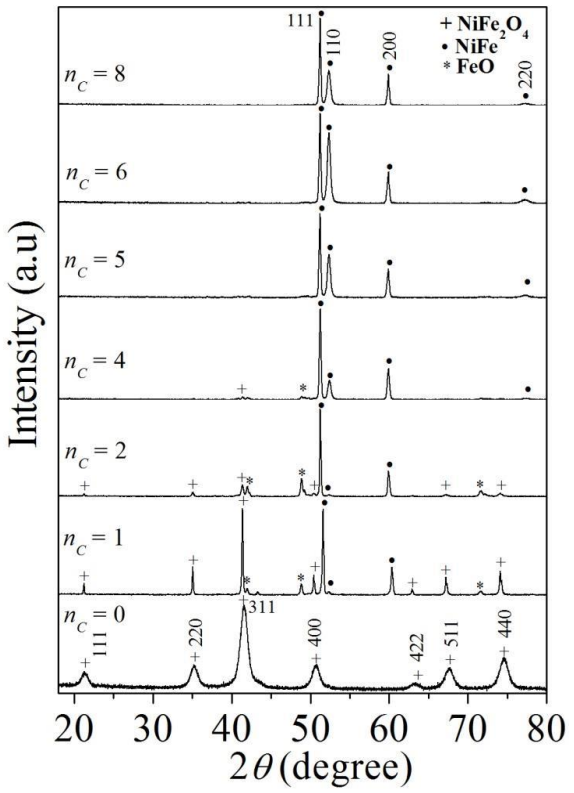

Figure 1. XRD patterns of $NiFe_2O_4$ reduced with n_c = 0, 1, 2, 4, 5, 6 and 8.

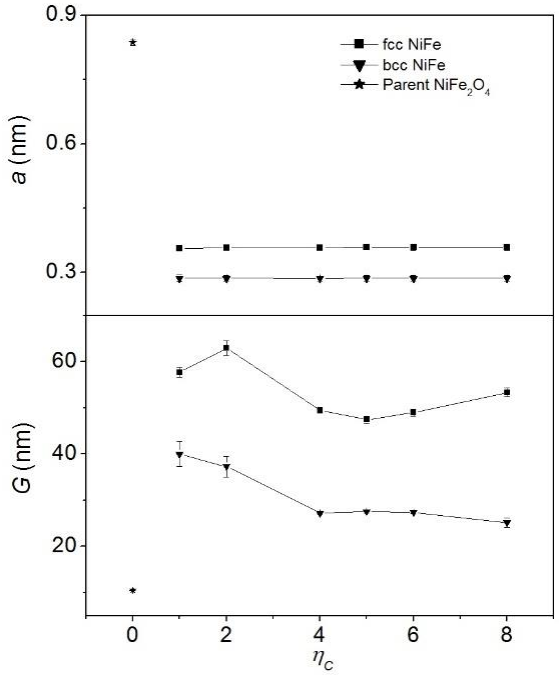

Figure 2. Variations of crystallite size G and lattice parameter a of the parent $NiFe_2O_4$, the bcc and fcc phases of the reduced samples at different amounts of activated charcoal n_c.

while that of the fcc phase is larger. The coexistence of the bcc and fcc phases give these nanocomposites and nano-alloys a plasticity and lattice resistance to deformation advantage because fcc structure favors plasticity while bcc structure favors lattice resistance to deformation [11]. Such NiFe particles have a higher resistance to oxidation than separate Fe and Ni particles [9]. The average values are close to the reported values of 2.87 Å and 3.52 Å respectively [5, 9].

The surfaces of the as-prepared nano-ferrite, nanocomposites formed at n_c = 2 and nano-alloys formed at n_c = 5 and 6 were examined by high resolution scanning electron microscope HRSEM as shown in Figure 3. The as-prepared sample is observed to consist of rough spherical particles which are less compact compared to the reduced samples. The nanocomposites are more compact with significant growth in the size of the particles. For n_c = 5 and 6 the particles are more closely packed which we attribute to the presence of the NiFe nano-alloy phase with higher density due to the presence of the fcc phase [10]. Similar images but less compacted were observed for FeNi alloy synthesized by chemical co-precipitation method [8].

^{57}Fe Mössbauer spectra measurements were performed at room temperature. The fitted Mössbauer spectra for n_c = 0, 5 and 6 are presented in Figure 4. Table 1 gives the values of the fitted parameters. The error function χ^2 provides an estimation of the fitting. Using the covariance matrix model in the Recoil fitting program, values of χ^2 of about one or less indicate better fits. The doublets in the reduced samples account for the coordination of Fe^{3+} and Fe^{2+} at both sites. The as-prepared $NiFe_2O$ Mössbauer spectrum was best fitted with two sextets corresponding to tetrahedral A- and octahedral B-sites. The hyperfine magnetic field B_{hf} values of 239 kOe and 420 kOe are consistent with α-Fe with comparable isomer shifts δ of 0.339 mm/s and 0.272 mm/s associated with Fe^{3+} ions [8, 12, 13]. The slightly smaller value of the isomer shifts at B-sites is due to larger covalency. The low quadrupole splitting values at both sites is indicative of the cubic symmetry around the Fe^{3+} ions [14]. The added doublet D accounts for the superparamagnetic relaxation effects due to the nano-size of the sample. Three sextets

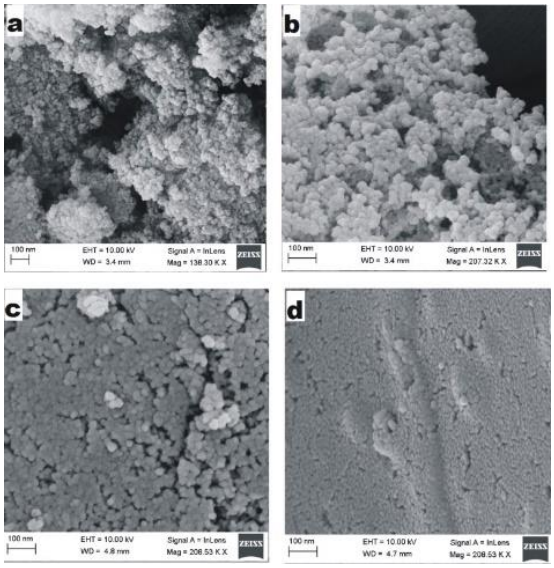

Figure 3. HRSEM images of: (a) the as-prepared $NiFe_2O_4$, (b) $NiFe_2O_4$/NiFe at n_c = 2, (c) NiFe at n_c = 5 and (d) NiFe at n_c = 6.

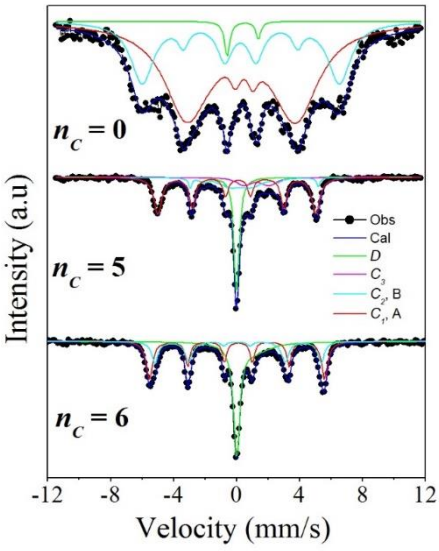

Figure 4. Mössbauer spectra of $NiFe_2O_4$ reduced with different amounts of activated charcoal n_c = 0, 5 and 6.

Table 1 Mössbauer parameters include hyperfine field (B_{hf}), isomer shifts (δ), quadrupole splitting (Δ_{EQ}), line widths (Γ), fraction populations (f) and reduced chi^2 (χ^2) of Fe ions of the as-prepared sample and alloy composite at n_c = 5 and 6 of activated charcoal.

n_C	Sub-pattern	B_{hf} (kOe) ±3	δ (mm/s) ±0.009	Δ_{EQ}(mm/s) ±0.002	Γ(mm/s) ±0.01	f (%) ±0.6	χ^2
0	A	293	0.339	0.005	0.58	68.0	0.7825
	B	420	0.272	0.014	0.49	30.0	
	D	-	0.420	2.150	0.23	1.9	
5	C_1	339	0.049	-0.048	0.19	39.5	1.3207
	C_2	325	0.900	-0.737	0.44	11.3	
	C_3	274	0.786	0.455	1.16	24.1	
	D	-	-0.017	0.139	0.22	25.0	
6	C_1	345	0.067	-0.042	0.16	35.1	0.9815
	C_2	327	0.053	0.032	0.19	24.5	
	D	-	0.540	1.080	-	40.4	

C_1, C_2 and C_3 are required to fit the spectra for n_c = 5 and two sextets C_1 and C_2 for n_c = 6 which we associate with the bcc and fcc phases. The high field components C_1 has a B_{hf} value of 339 kOe and 345 kOe which is attributed to the bcc FeNi and the lower field components C_2 has a value of 325 kOe and 327 kOe attributed to the fcc phase [10, 15] for n_c = 5 and 6, respectively. Sextet C_3 accounts for the small mixed phase denominated by fcc phase with a B_{hf} value of 274 kOe. These results are close to reported values of 343 kOe, 320 kOe and 273 kOe for FeNi alloy [8, 10, 16]. The isomer shift values obtained for the fully reduced samples are significantly different and appear to confirm change from Fe^{3+} to Fe^{2+} [17].

Room temperature magnetic hysteresis loops of the parent sample, nanocomposites and NiFe nano-alloys recorded in applied magnetic fields of up to 50 kOe are presented in Figure 5. Magnetic properties such as coercivity (H_C) and saturation magnetization (M_S) were calculated from the hysteresis loops. The samples exhibit soft magnetic hysteresis loops and the maximum magnetization

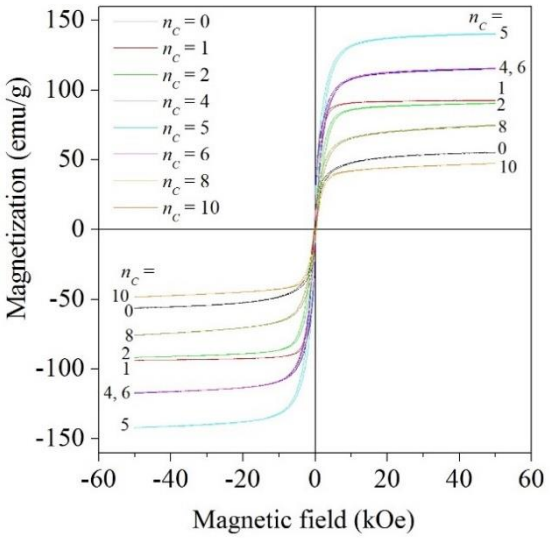

Figure 5. Magnetic hysteresis loops for the as-prepared $NiFe_2O_4$, $NiFe_2O_4$/NiFe nanocomposites and NiFe nano-alloy samples measured at room temperature.

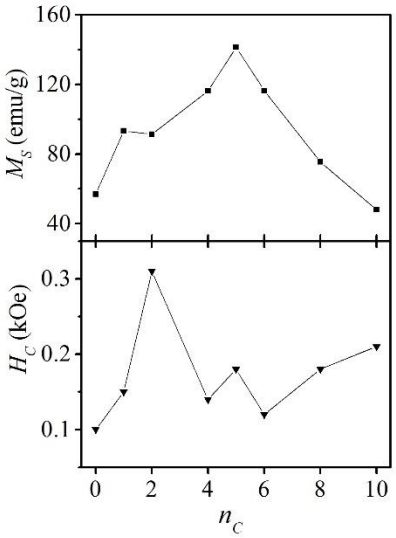

Figure 6. Variations of saturation magnetization M_S and coercivity H_C with n_c.

at a magnetic field of 50 kOe is herewith regarded as the estimate for saturation magnetization at a particular temperature. The as-prepared nano-ferrite has a coercivity of 0.10 kOe and saturation magnetization of 57 emu/g. The variations of the magnetization and coercivity with ratios of activated charcoal n_c are presented in Figure 6. The reduction of $NiFe_2O_4$ nano-ferrite appears to enhance the magnetizations and coercive fields. The fluctuating variation of the coercivity is not quite clear. The magnetization attains a maximum value of 141 emu/g at n_c = 5 while the coercive field has a maximum of 0.31 kOe at n_c = 2. For n_c > 5 magnetization decreases which we associate with the onset of the NiFe bcc and fcc phases with weaker internal hyperfine fields as deduced from Mössbauer spectroscopy. Higher magnetization and coercive fields are therefore obtained in the $NiFe_2O_4$/NiFe nanocomposites which begin to decline as inter metallic NiFe phase begins to dominate more and more. Low temperature measurements were also performed on a mini cryogen free measurement system. Typical hysteresis loops obtained at 4 K are presented in Figure 7. Figure 8 shows the coercivity and saturation magnetization dependence on temperature. The magnetizations are observed to increase gradually with decreasing temperature. A more significant increase in coercive fields is observed in the $NiFe_2O_4$ nano-ferrite which appears to follow the typical behavior for the spinel ferrites [4]. The nanocomposite sample $NiFe_2O_4$/NiFe at n_c = 4 had the highest magnetization below about 100 K compared to the parent nano-ferrite or fully reduced sample. The coercivity of the NiFe nano-alloy seems to be slightly affected by temperature change compared to the nanocomposite or the $NiFe_2O_4$.

4. Conclusions

Nanocomposites of $NiFe_2O_4$/NiFe and NiFe nano-alloy were synthesized by the reduction of $NiFe_2O_4$ using activated charcoal n_c. XRD measurements showed NiFe nano-alloy for n_c = 5 and 6. The peaks for the reduced samples were indexed to the bcc α-Fe and fcc γ-Fe lattices for the NiFe nano-alloy. Fitted Mössbauer analysis for n_c = 5 and 6 show high hyperfine magnetic fields associated with the bcc phase while the lower field component is associated with the fcc phase of NiFe. The isomer shift values indicate change to Fe^{2+} from Fe^{3+} in the spinel phase. The surface morphology for n_c = 5 and 6 have their particles closely packed and compacted which we attribute to the presence of NiFe alloy phase with high density of fcc packing. Room temperature measurements of magnetization showed enhanced saturation magnetizations. The coercivity of NiFe is less dependent on temperature.

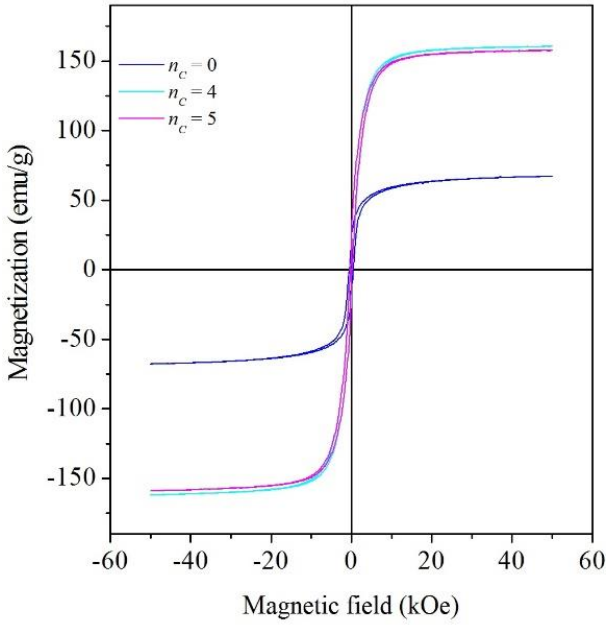

Figure 7. Magnetic hysteresis loops for as-prepared $NiFe_2O_4$ nano-ferrite, $NiFe_2O_4$/NiFe nanocomposite and NiFe nano-alloy samples measured at 4 K.

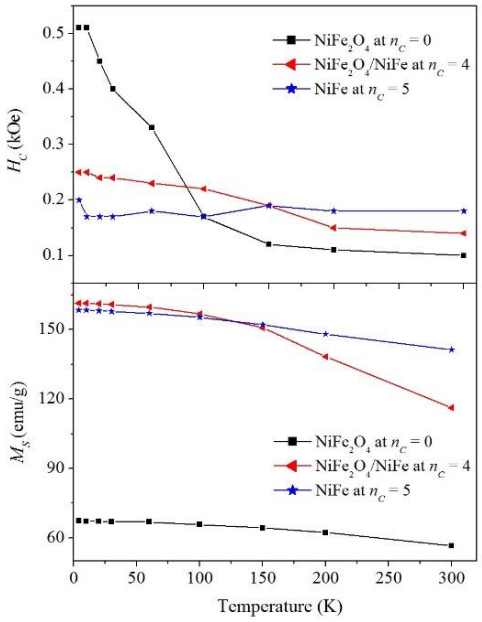

Figure 8. Coercivity H_C and saturation magnetization M_S dependence on temperature T for as-prepared $NiFe_2O_4$ nano-ferrite, $NiFe_2O_4$/NiFe nanocomposite and NiFe nano-alloy.

Acknowledgments

We express our gratitude to the National Research Foundation (NRF), South Africa for the NNEP grant for the VSM equipment, EM unit (UKZN, WC) for HRTEM and HRSEM.

References

[1] Sivakumar P, Ramesh R, Ramanand A, Ponnusamy S and Muthamizhchelvan C 2011 *J. Mater. Res*. **46** 2204
[2] Liu X G, Geng D Y, Choi C J and Kim J C 2009 *J. Nanopart. Res*. **11** 2097–2104
[3] Zhang Y, Zuo T, Cheng Y and Liaw P K 2013 *J. Sci. Rep*. **38** 1455
[4] Mazz K, Mumtaz A, Hasanain S K and Bertino M F 2010 *J. Magn. Magn. Mater*. **322** 2199–2202
[5] Rawwagah F H, Lehlooh A F, Mahmood S H, Mahmoud S, El-Ali A R, Said M R, Odeh I and Abu-Aljarayesh I 2012 *Jord. J. Phys*. **5** 9–14
[6] Hu R J and Chen A 2012 *J. Advn. Mater. Res*. **486** 65–69
[7] Abdallah H M I and Moyo T 2013 *J. Alloys Comp*. **562** 156–163
[8] Dong X L, Zhang Z D, Zhao X G and Chuang Y C 1999 *J. Mater. Res*. **14** 398–406
[9] Valderruten J F, Pérez A G A and Grenéche J M 2008 *J. Appl. Phys. Condens. Mater* **20** 485304
[10] Zhang Y, Zuo T, Cheng Y and Liaw P K 2013 *J. Sci. Rep*. **38** 455
[11] Leite G C P, Chagas E F, Pereira R, Prado R J, Terezo A J, Alzamora M and Saitovitch E B 2012 *J. Magn. Magn. Mater*. **324** 2711–2716
[12] Guittoum A, Layadi A, Tafat H, Bourzam A, Souam N and Lenoble O 2009 *J. Phil. Magn.* **88** 1085–1098
[13] Umare S S, Ningthoujam R S, Sharma S J, Kurian S S S and Gajbhiye N S 2008 *Hyperfine Interact*. **184** 235–243
[14] Rodriguez R R, Valenzuela J L and Tabares J *A Hyperfine Interact*. DOI 10.1007/s10751-013-0834-5.
[15] Lehlooh D A and Mahmood H S 2002 *Hyperfine Interact*. **139-140** 387–392
[16] Hassan M Y, El-Desoky M M, Masuda H, Kubuki S and Nishida T *Hyperfine Interact*. DIO 10.1007/s10751-011-0478-2
[17] Chunhui D, Gaoxue W, Dangwei G, Changjun J and Desheng X 2013 *Nanoscale Res. Lett*. **8** 196